The Rotation Curve, Mass Distribution, and Dark Matter Content of the Milky Way from Classical Cepheids

Iminhaji Ablimit[1,2,4] , Gang Zhao[1] , Chris Flynn[3] , and Sarah A. Bird[1]
[1] Key Laboratory for Optical Astronomy, National Astronomical Observatories, Chinese Academy of Sciences, Beijing 100012, China; iminhaji@nao.cas.cn, iminhaji@kusastro.kyoto-u.ac.jp, gzhao@nao.cas.cn
[2] Department of Astronomy, Kyoto University, Kitashirakawa-Oiwake-cho, Sakyo-ku, Kyoto 606-8502, Japan
[3] Centre for Astrophysics and Supercomputing, Swinburne University of Technology, P.O. Box 218, Hawthorn, VIC 3122, Australia; cflynn@swin.edu.au

Abstract

With the increasing number of large stellar survey projects, the quality and quantity of excellent tracers for studying the Milky Way are rapidly growing, one of which is the classical Cepheids. Classical Cepheids are high-precision standard candles with very low typical uncertainties ($<3\%$) available via the mid-infrared period–luminosity relation. About 3500 classical Cepheids identified from the Optical Gravitational Lensing Experiment, All-Sky Automated Survey for Supernova, Gaia, Wide-field Infrared Survey Explorer, and Zwicky Transient Facility survey data have been analyzed in this work, and their spatial distributions show a clear signature of Galactic warp. Two kinematical methods are adopted to measure the Galactic rotation curve (RC) in the Galactocentric distance range of $4 \lesssim R_{\mathrm{GC}} \lesssim 19$ kpc. Gently declining RCs are derived by both the proper motion (PM) method and three-dimensional velocity vector (3DV) method. The largest sample of classical Cepheids with the most accurate 6D phase-space coordinates available to date are modeled in the 3DV method, and the resulting RC is found to decline at the relatively smaller gradient of (-1.33 ± 0.1) km s^{-1} kpc^{-1}. Comparing to results from the PM method, a higher rotation velocity ((232.5 ± 0.83) km s^{-1}) is derived at the position of the Sun in the 3DV method. The virial mass and local dark matter density are estimated from the 3DV method, which is the more reliable method, $M_{\mathrm{vir}} = (0.822 \pm 0.052) \times 10^{12} \, M_{\odot}$ and $\rho_{\mathrm{DM},\odot} = 0.33 \pm 0.03$ GeV, respectively.

Unified Astronomy Thesaurus concepts: Dark matter density (354); Galaxy mass distribution (606); Milky Way dark matter halo (1049); Milky Way dynamics (1051); Cepheid variable stars (218); Galaxy rotation curves (619); Dark matter (353)

1. Introduction

The mass distribution and dark matter density profiles of the Milky Way are not just key probes of its assembly history (e.g., Lake 1989; Read et al. 2008; Deason et al. 2019), but also provide crucial clues for the cosmological context of galaxy formation (e.g., Dubinski 1994; Ibata et al. 2001; Lux et al. 2012). The two distributions are usually studied in the frame work of the "standard" Cold Dark Matter model (ΛCDM for short, where the Λ refers to the density of "dark energy"). In this cosmological model, the energy density of the universe comprises approximately 5% of baryons, 27% of dark matter, and 68% of dark energy. The rotation (or circular velocity) curve measurement is a classical way to deliver an indirect measurement of these profiles of the Milky Way (Volders 1959; Freeman 1970; Bosma & van der Kruit 1979; van Albada et al. 1985; Sofue et al. 2009).

Specifically, the Galactic rotation curve (RC) is the mean circular velocity around the center of the Galaxy as a function of galactocentric distance measured in the disk midplane. The RC has been derived with various methods and various tracer objects moving in the gravitational potential of the Galaxy (e.g., Wilkinson & Evans 1999; Weber & de Boer 2010; Sofue 2012; Nesti & Salucci 2013). For example, the RC of the Galactic

inner region has been derived by the tangent-point method associated with H I regions (Gunn et al. 1979; Levine et al. 2008; Sofue et al. 2009). Comparing to the tangent-point method, methods using stars, dwarf galaxies, or globular clusters with distances and at least one of the velocity components (radial velocity and/or proper motions, PMs) are considered to be the better measurement for the Galactic (inner and outer region) RC (e.g., Honma et al. 2007; Smith et al. 2007; Bovy et al. 2012; Bovy & Rix 2013; Bhattacharjee et al. 2014; Kafle et al. 2014; Reid et al. 2014; Bowden et al. 2015; Ablimit & Zhao 2017; Binney & Wong 2017; Pato & Iocco 2017; Russeil et al. 2017; Katz et al. 2018; Monari et al. 2018; Sohn et al. 2018). Recently, the measured number of tracers with accurate six-dimensional (6D) phase-space information is increasing rapidly, with the growing numbers of sky surveys, such as Sloan Digital Sky Survey (SDSS), Gaia, Wide-field Infrared Survey Explorer (WISE), Zwicky Transient Facility (ZTF), Optical Gravitational Lensing Experiment (OGLE), ASAS, Gaia-ESO, APOGEE, etc., and these data enable us to more precisely measure RCs.

Certain types of variable stars are excellent distance indicators due to well-known period–luminosity relations. Thus, they are taken as excellent objects to study the structure, kinematics, and dynamics of the Galaxy, such as RR Lyrae stars (Ablimit & Zhao 2017, 2018; Medina et al. 2018; Utkin et al. 2018; Wegg et al. 2019) and Cepheids (e.g., Kawata et al. 2018). Frink et al. (1995) derived the Galactic RC from the proper motion (PM) of 144 Cepheids. Subsequently, Pont et al. (1997) constructed the RC of the Galaxy from radial velocities of 48 classical Cepheids distributed in the outer disk region

---

[4] LAMOST Fellow.

between the Galactocentric distances 10 and 15 kpc. Gnaciński (2019) obtained the RC by adopting three kinematic approaches by using 160, 228, and 120 classical Cepheids from the catalog of Mel'nik et al. (2015). They showed that the slope of the RC lies between a flat RC and a Keplerian RC. However, Mróz et al. (2019) tracked the RC from the 6D phase-space information of 773 classical Cepheids, and they found a relatively flat RC. They did not estimate mass distribution and dark matter content of the Milky Way.

In this work, we have selected and analyzed about 3500 classical Cepheids that have precise distances and measured the Milky Way RC using the PM method (Gnaciński 2019) and 3D velocity vector method (Reid et al. 2009). In Section 2, we introduce the classical Cepheids data collected for this work. Two methods to calculate the rotation velocities of classical Cepheids are introduced, and the resulting RC and its constraint on the mass and dark matter profile of our Galaxy are given and discussed in Section 3. The concluding remarks are presented in Section 4.

2. Data Selection

We collected our sample from several classical Cepheids catalogs as follows: the All-Sky Automated Survey for Supernovae (ASAS-SN) variable stars catalog (Shappee et al. 2014; Jayasinghe et al. 2018), the classical Cepheid sample by Skowron et al. (2019a, 2019b) basically from OGLE (Udalski et al. 2015, 2018), classical Cepheids from the European Space Agency (ESA) mission Gaia (Gaia Collaboration et al. 2016, 2018; Ripepi et al. 2019), and the classical Cepheids catalog by Chen et al. (2019) from WISE (Wright et al. 2010). We added new classical Cepheids identified from the ZTF catalog (Bellm et al. 2019) by Chen et al. (2020). We made a cross-match of all the Cepheids from different catalogs in order to remove multiple entries. Then, we selected Cepheids that have mid-infrared ($W1$, $W2$, $W3$, and $W4$ band) magnitudes from the AllWISE catalog. We calculated heliocentric distances (D_h) based on the relations given in Wang et al. (2018) with the $W1$, $W2$, $W3$, and $W4$ bands, and took average values for each Cepheid (also see Skowron et al. 2019a for the same calculation method). Recently, it has been discussed that distances derived from mid-infrared period–luminosity relations are more accurate than distances obtained from parallaxes (e.g., Mróz et al. 2019). After deriving distances, we keep classical Cepheids with $|z| \leqslant 4$ kpc, and we have 3483 classical cepheids (Galactic longitude (l) and latitude (b) distributions are shown in the upper left panel of Figure 1): 2223 of them from Skowron et al. (2019a, 2019b; magenta stars and red circles), 160 from the ASAS-SN catalog (blue squares), 303 from the Gaia catalog (open violet left triangles), 167 from Chen et al. (2019; green triangles), 618 of them are from Chen et al. (2020; black triangles).

The spatial distributions are shown in Figure 1, and all distributions show the clear Galactic warp that is reported by Skowron et al. (2019a, 2019b) and Chen et al. (2019). The 3D positions of Cepheids and galactocentric distances (r) in the Cartesian coordinate system are calculated as $x = R_\odot - D_h \cos b \cos l$, $y = D_h \cos b \sin l$, $z = D_h \sin b$, and $r = \sqrt{x^2 + y^2 + z^2}$, where $R_\odot$ is the distance from the Sun to the Galactic center, and the recent most accurate value, 8.122 ± 0.031 kpc (Gravity Collaboration et al. 2018), is adopted. The projection of galactocentric distance on the Galactic plane (R) is

as follows:

$$R = \sqrt{x^2 + y^2}. \tag{1}$$

3. Modeling the Rotation Curve

3.1. The Halo Model

The rotation velocity at a radius R from the center of an axisymmetric mass distribution is related to the total gravitational potential within R and mass $M(<R)$ (at $z \sim 0$),

$$V_c^2(R) = R\frac{\partial \Phi}{\partial R} = \frac{GM(<R)}{R}, \tag{2}$$

where Φ and G are the gravitational potential and gravitational constant, respectively. If we consider the bulge, thin disk, thick disk, and dark matter halo for the Galactic potential, which for the respective contributions are $\Phi_{\rm bulge}$, $\Phi_{\rm thin}$, $\Phi_{\rm thick}$, and $\Phi_{\rm halo}$,

$$\Phi(R, z) = \Phi_{\rm bulge}(r) + \Phi_{\rm thin}(R, z) + \Phi_{\rm thick}(R, z) + \Phi_{\rm halo}(r), \tag{3}$$

and velocity contributions to the RC from different components are given by

$$V_c^2(R) = V_{\rm bulge}^2(R) + V_{\rm thin}^2(R) + V_{\rm thick}^2(R) + V_{\rm halo}^2(R). \tag{4}$$

The Navarro–Frenk–White (NFW) model (Navarro et al. 1996, 1997) that is derived from the simulations in the CDM scenario of galaxy formation has been widely used for modeling the dark matter halo (e.g., Sofue 2012; Wang et al. 2018). We assume that density distributions of all stellar components are well known, and the velocity contribution of the dark matter halo is fitted by searching for the best parameters by using the Markov Chain Monte Carlo method. For the fitting model, the Miyamoto–Nagai potential model (Miyamoto & Nagai 1975) and a spherical Plummer potential (Plummer 1911) are used for the thin/thick disks and bulge, respectively. We take the parameter values of the enclosed mass, the scale length, and the scale height from model I of Pouliasis et al. (2017).

The NFW dark matter density profile is described as

$$\rho(r) = \frac{\rho_{\rm crit} \delta_c}{(r/r_s)(1 + r/r_s)^2}, \tag{5}$$

where $\rho_{\rm crit} = 3H^2/8\pi G$, and $H = 70.6$ km s^{-1} Mpc^{-1} is taken for the Hubble constant. The quantity of δ_c is the characteristic overdensity of the halo. Here, $r_s = R_{\rm vir}/c$ is the scale radius, where c is so-called concentration parameter, and $R_{\rm vir}$ is the virial radius. $R_{\rm vir}$ is related to the virial mass as $M_{\rm vir} = 200\rho_{\rm crit}\frac{4\pi}{3}R_{\rm vir}^3$ (see Navarro et al. 1996, 1997 for more details). In the next subsections, the RCs from different kinematical models and fitting results are discussed.

3.2. The Rotation Curve from Proper Motions

After measuring the PM of the star and setting the solar rotation speed as $V_{c,\odot} = 233.6 \pm 2.8$ km s^{-1} (Mróz et al. 2019), and then assuming a circular orbit for the Cepheid, the following
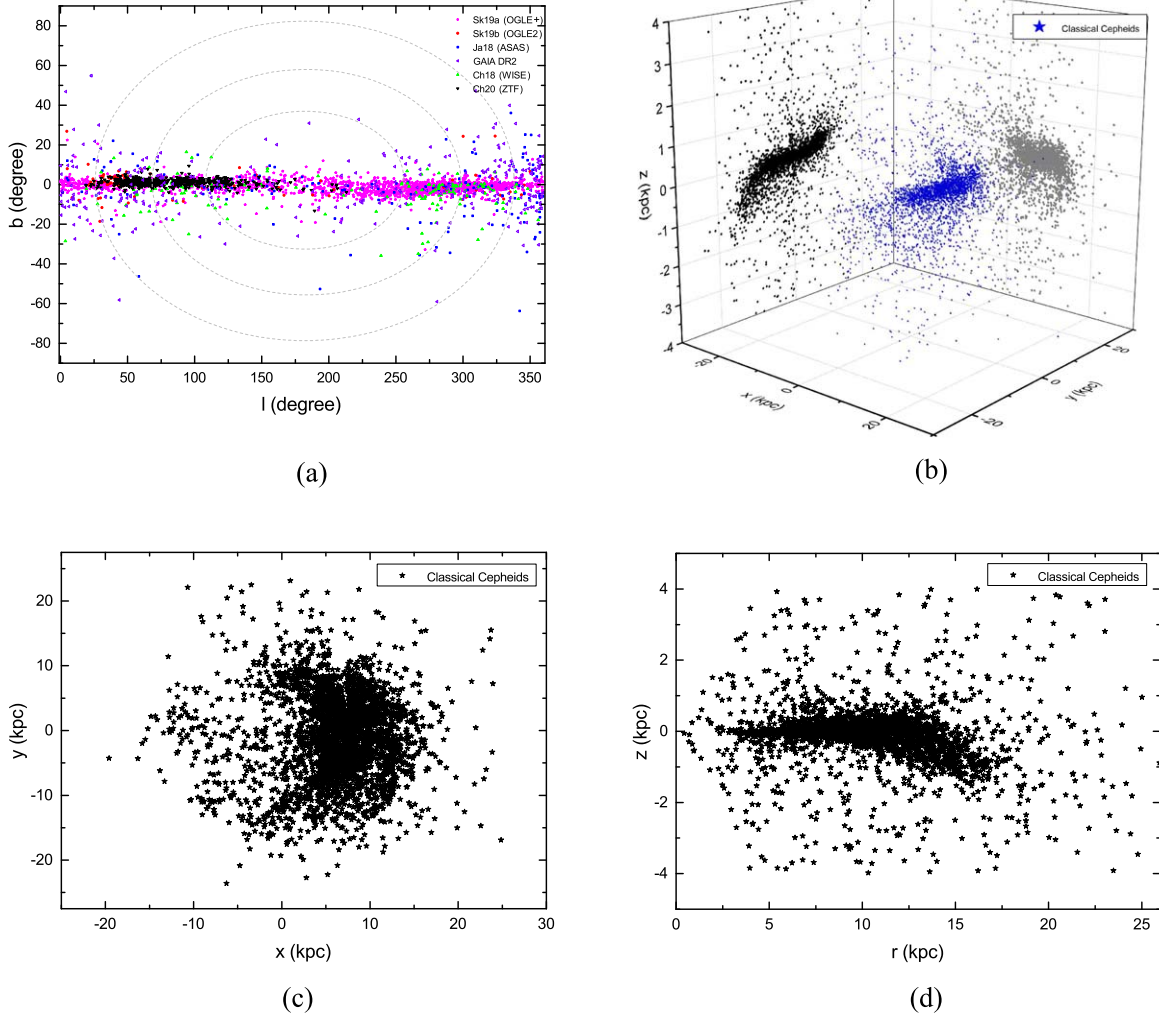
(a)

(b)

(c)

(d)

Figure 1. Distributions of the Galactic longitude (l) and latitude (b), and spatial distributions. The 3D positions, projections in the x–z and y–z planes, are shown in the upper right panel; projections in the x–y and r–z planes are given in the lower left and lower right panels, respectively.

formula gives the rotation velocity (Gnaciński 2019):

$$V_c = \frac{R}{R_\odot \cos l - D}(V_t + V_{c,\odot}\cos l), \quad (6)$$

where the transverse velocity $V_t = D\mu_l$, and μ_l is the PM in the Galactic longitude (multiplied by $\cos b$). The stars with $|z| > 0.5$ kpc are excluded, and unphysical velocities caused by small or negative denominators are removed (see Gnaciński 2019 for the same selection criterion), so only 591 classical Cepheids are left from whole classical Cepheids for this kinematical modeling. Among our sample, there are 168, 324, and 411 classical Cepheids distributed in the Galactocentric range of $R > 12$ kpc, $R > 10$ kpc, and $R > 8$ kpc, respectively. Figure 2 shows μ_l and the calculated rotation velocities of 591 classical Cepheids. More than 98% of μ_l have uncertainties less than 0.2 mas yr^{-1}, and this leads to small uncertainties in the rotation velocity calculation. The number of analyzed classical Cepheids in this work is about twice that used in Gnaciński (2019), and we have more stars in the outer disk, which is helpful for improving the accuracy of the RC measurement.

Figure 3 shows the rotation velocity distribution from $R = 4$ and 19 kpc (see Table 1 for the values), and the linear function fitted from it is

$$V_c(R) = (222.91 \pm 2.08)\,\text{km s}^{-1}$$
$$+ (-1.45 \pm 0.16)\,\text{km s}^{-1}\,\text{kpc}^{-1} \times (R - R_\odot). \quad (7)$$

This yields a gently declining RC with a small gradient of (-1.45 ± 0.16) km s^{-1} kpc^{-1}, and indicates the rotation velocity at the position of the Sun as $V_c(R_\odot) = 222.91 \pm 2.08$ km s^{-1}. By fixing the contributions of baryonic components of the Galaxy (see model I of Pouliasis et al. 2017), we estimated the mass and the properties of the Milky Way's dark matter halo with the NFW profile (fitted results in Figure 3), and we derived $M_{\text{vir}} = (6.63 \pm 0.67) \times 10^{11}\,M_\odot$, corresponding to a virial radius $R_{\text{vir}} = 178.57 \pm 5.42$ kpc. We obtained the concentration of $c = 12.36 \pm 0.42$ and a scale radius of $r_s = 14.45 \pm 0.46$ kpc. The indicated characteristic density is $\rho_0 = (1.05 \pm 0.12) \times 10^7\,M_\odot\,\text{kpc}^{-3}$, and dark matter density at the location of the Sun is $\rho_{\text{DM},\odot} = 0.28 \pm 0.04$ GeV cm^{-3} (units of GeV cm^{-3} may be seen more in particle physics; for astronomers, there is a useful conversion: $0.008 M_\odot\,\text{pc}^{-3} = 0.3\,\text{GeV cm}^{-3}$).
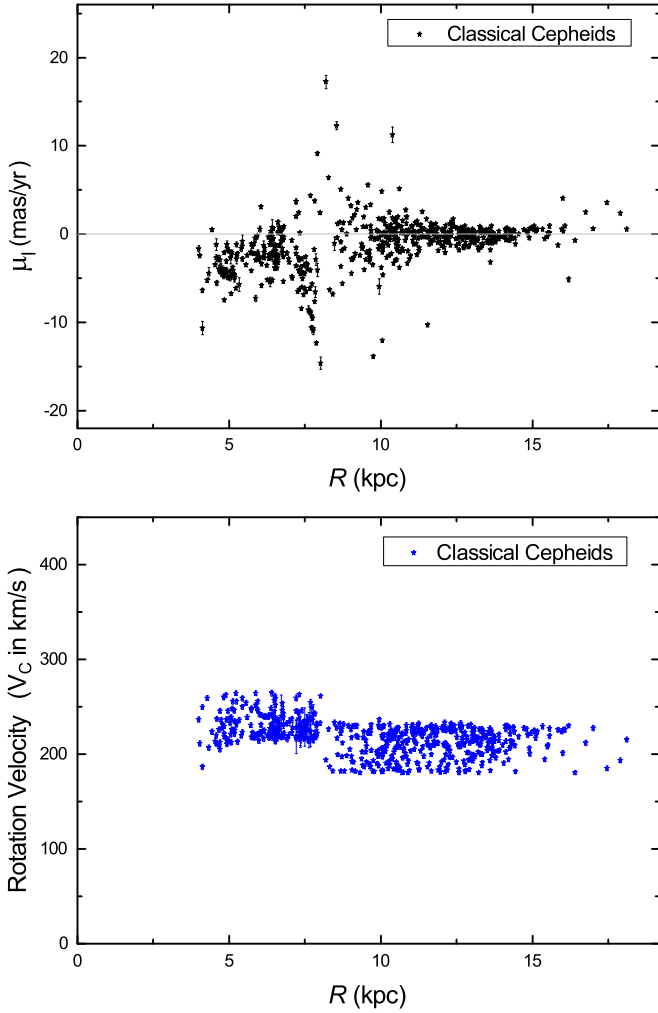
Figure 2. Distributions of proper motions and derived rotation velocities in the proper motion model.

3.3. The Rotation Curve from the 3D Velocity Vector

The rotation velocity can also be determined from the 3D velocity vector if the three quantities of radial velocity and PMs are available. Reid et al. (2009) described the calculation formulas of stellar motions by using radial velocity (V_h) and PMs, which we adopt here: U-velocity component toward the Galactic center, V-velocity component along with the Galactic rotation, and W toward the North Galactic pole. The optimizing model of $V_c(R) = V_{c,\odot} + \frac{dV_c}{dR}(R - R_\odot)$, where $V_{c,\odot}$ and $\frac{dV_c}{dR}$ are the Sun's rotation velocity and fitted parameter, is adopted for deriving rotation velocities (see Reid et al. 2009 for more details). For the peculiar (noncircular) solar motions with respect to the local standard of rest, the values of $U_\odot = 11.1 \pm 1.3$ km s^{-1}, $V_\odot = 12.24 \pm 2.1$ km s^{-1}, and $W_\odot = 7.3 \pm 0.7$ km s^{-1} are taken from Schönrich et al. (2010).

The PMs of the sample are obtained from Gaia DR2, and the radial velocities are derived by cross-matching with Gaia DR2 and LAMOST DR6 data (e.g., Zhao et al. 2006, 2012). We excluded five Cepheids known in the binary systems, and we put extra constraints of $|z| \leqslant 2.0$ kpc and radial velocity uncertainty <20 km s^{-1} to remove 11 objects in order to reduce uncertainties. It is well known that the radial velocity uncertainty may be larger
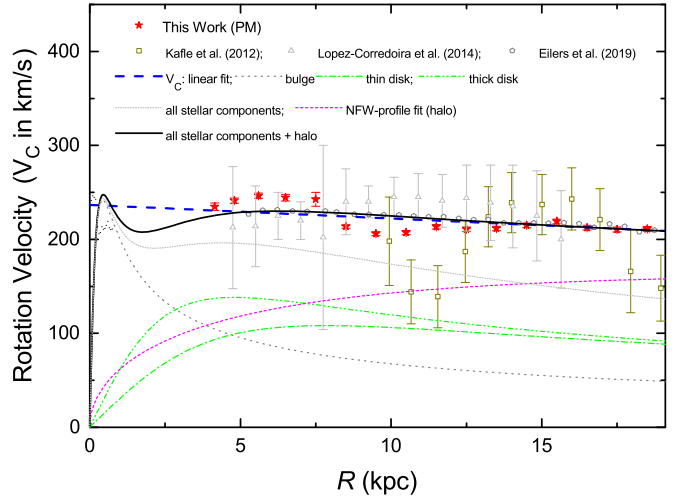

Figure 3. Red stars show the distribution of new measured rotation velocities of the Milky Way from the proper motion method, and the error bars are derived existing errors of the sample without including the systematic uncertainties. The blue dashed line is the linear fit to the new data in this work. The black solid line is the best fit to the rotation velocity with an assumption that the Milky Way components are the bulge (gray dotted line), thin disk (green dashed–dotted line), thick disk (green dashed–dotted–dotted line), and dark matter halo (magenta short dashed line) by the NFW profile. The light gray short-dotted line represents the fit to the rotation velocity modeled as the sum of all stellar components. The best fit to the rotation velocity curve modeled as the sum of all components of the Milky Way is shown by the black solid line. Three other symbols with different colors demonstrate the rotation velocities taken from three previous works for the comparison.

for a single star when it is measured near the pulsation phase (Stibbs 1955). However, the uncertainties of variable stars caused by the pulsation need further investigations, and it may not clearly affect the statistical result (see Ablimit & Zhao 2017). For the 3D velocity model, we have 1078 classical Cepheids: 836 of them from Skowron et al. (2019a, 2019b), 55 from ASAS-SN catalog, 73 from Gaia DR2 Cepheids catalog, 22 from Chen et al. (2019), and 92 from Chen et al. (2020). Among our sample, there are 47, 165, 377, and 659 classical Cepheids distributed in the Galactocentric ranges of $R > 14$ kpc, $R > 12$ kpc, $R > 10$ kpc, and $R > 8$ kpc, respectively. In this work, the farthest distance is up to ~19 kpc, simply because no star satisfies the criterion to model beyond 19 kpc. The radial velocities of 1043 stars are derived from the Gaia DR2 catalog while 35 of them are obtained from LAMOST DR6.

Cleaned Sample. There are likely some objects in the 1078 star sample that may be members of binary systems (and unrecognized with incorrect astrometric solutions) or categorized erroneously as classical Cepheids that as such and may actually be another type of variable. There are also some classical Cepheids with observed velocity components of about 4σ (σ is the dispersion of residuals) larger than the mean. Considering these possibilities and uncertainties, we selected 963 classical Cepheids from the 1078 stars as the cleaned sample, and derived rotation velocities of the cleaned sample are shown in Table 1. The measured RCs from the cleaned sample and the all 1078 sample can be fitted by the same linear function.

The distributions of V_h, μ_l, and μ_b and rotation velocities are given in Figure 4. The RC from the 3D velocity vector (Figure 5) is well approximated by the following linear
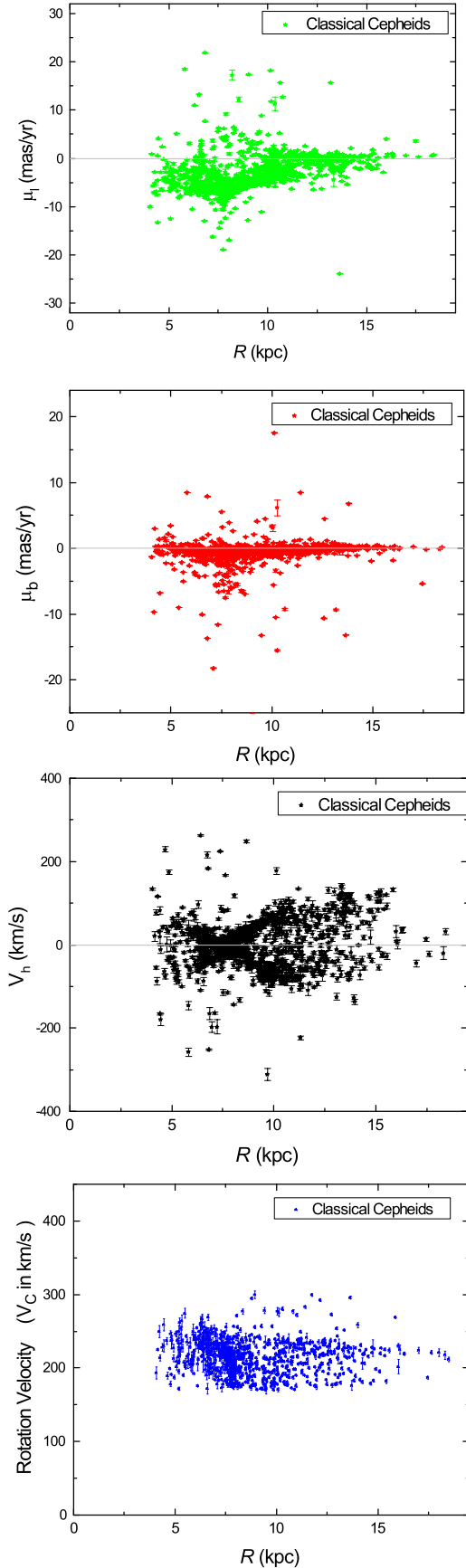
Figure 4. Distributions of the proper motions in the Galactic longitude direction, proper motions in the Galactic latitude direction, and radial velocities used in the 3D velocity vector method. The calculated rotation velocities of individual stars are also shown in the figure.

function:

$$V_c(R) = (232.5 \pm 0.83)\,\mathrm{km\,s^{-1}}$$
$$+ (-1.33 \pm 0.1)\,\mathrm{km\,s^{-1}\,kpc^{-1}} \times (R - R_\odot). \quad (8)$$

The RC from this method is gently decreasing with a derivative of (-1.33 ± 0.1) km s^{-1} kpc^{-1}. The slope of the curve and the rotation velocity at the location of the Sun ($V_c(R_\odot) = 233.5 \pm 0.83$ km s^{-1}) are in a good agreement with the results of Mróz et al. (2019), as about 70% of data points in the sample overlap with that of Mróz et al. (2019). However, there are more than 300 different stars in this work. In particular, our sample has more stars in the outer disk, which improves the accuracy of the RC, and is helpful to put more accurate constraints on the distribution of dark matter in the Milky Way. Comparing to the virial mass from the PM method, we derived a higher virial mass in this method, $M_{\mathrm{vir}} = (8.22 \pm 0.52) \times 10^{11}\, M_\odot$, with a corresponding virial radius $R_{\mathrm{vir}} = 191.84 \pm 4.12$ kpc. The resulting concentration and scale radius are $c = 13.04 \pm 0.34$ and $r_s = 14.71 \pm 0.42$ kpc, respectively. The estimated characteristic density and dark matter density at the location of the Sun are $\rho_0 = (1.20 \pm 0.1) \times 10^7\, M_\odot\,\mathrm{kpc^{-3}}$ and $\rho_{\mathrm{DM},\odot} = 0.33 \pm 0.03$ GeV cm^{-3}, respectively.

3.4. Comparison and Discussion

There are 366 common classical Cepheids modeled in the two methods, and different tracers are selected due to different criteria for different methods. The discrepancy of the two methods' results are within 10%. The most important advantage of our sample is the accuracy of the distances that have uncertainties at a level of 2%–3%. We have small uncertainties in our results (see the values of uncertainties in Table 1); however, only bootstrapping uncertainties without the systematic uncertainties are considered in this work (see Eilers et al. 2019 for analysis of the possible systematic uncertainties). The effect of the asymmetric drift is not considered in the calculation of this work due to the very small systematic uncertainty it causes (e.g., estimated as ± 0.28 km s^{-1} by Kawata et al. 2018). Within 19 kpc, all systematic uncertainties added up (i.e., caused by uncertainties of distances, uncertainty of $R_\odot$, and the asymmetric drift, etc.) only affect the RC measurement at a $\lesssim 5\%$ level. It is well known that the motions of stars are affected by Galactic substructures (e.g., Grand et al. 2014; Bovy 2015; Kawata et al. 2018; Martinez-Medina et al. 2019). We did not use stars located at $R < 4.0$ kpc in order to reduce the influence of other structures like the Galactic bar.

The slopes of the RCs from two methods are gently decreasing, as favored by recent discoveries (e.g., Eilers et al. 2019; Mróz et al. 2019). They are not as flat as demonstrated in Sofue et al. (2009) and Reid et al. (2014), and it is not as steep as shown in Gnaciński (2019). This indicates that the dark matter content would not possibly be so high or so low as claimed in those previous works. The result (see the cross-point between the RC of all stellar components and dark matter halo in Figure 3) from the PM method suggests that the dark matter halo dominates the Galactic rotation when $R \gtrsim 14.5$ kpc, and this is in good agreement with recent finding by Eilers et al. (2019). However, based on the 3D velocity method (as shown in Figure 5), the dark matter halo dominates the rotation velocity if $R \gtrsim 12.5$ kpc. The comparison of the two velocity distributions from the two methods gives the same dip-like feature; there is a clear decline at a distance around ∼10 kpc,

Table 1
Measurements of the Galactic Rotation Velocity Based on Two Different Methods

Proper Motion Method			3D Velocity Method		
R (kpc)	V_C (km s^{-1})	σ_{V_C} (km s^{-1})|	R (kpc)	V_C (km s^{-1})	σ_{V_C} (km s^{-1})
4.2	234.11	3.96	4.56	230.15	7.15
4.8	241.24	2.75	5.32	234.93	8.01
5.6	246.45	2.61	6.11	237.41	5.97
6.5	244.43	3.49	6.97	236.21	4.67
7.5	242.69	7.35	7.78	234.02	3.77
8.5	213.65	1.91	8.59	232.51	2.68
9.5	206.04	2.03	9.33	231.42	2.17
10.5	207.26	2.21	10.11	231.61	1.99
11.5	213.31	2.39	10.88	229.08	1.95
12.5	210.75	2.37	11.67	226.93	2.04
13.5	211.49	2.38	12.36	226.61	1.55
14.5	214.88	2.49	13.04	225.63	2.11
15.5	219.08	2.58	13.86	226.36	1.61
16.5	212.45	2.49	14.61	225.87	2.21
17.5	210.62	2.62	15.42	226.13	2.09
18.5	211.14	2.42	16.26	223.29	2.56
			17.04	219.46	0.30
			17.87	210.68	2.72
			18.62	216.15	4.76

Note. For the 3D velocity method, the results of the cleaned sample are given in the table.
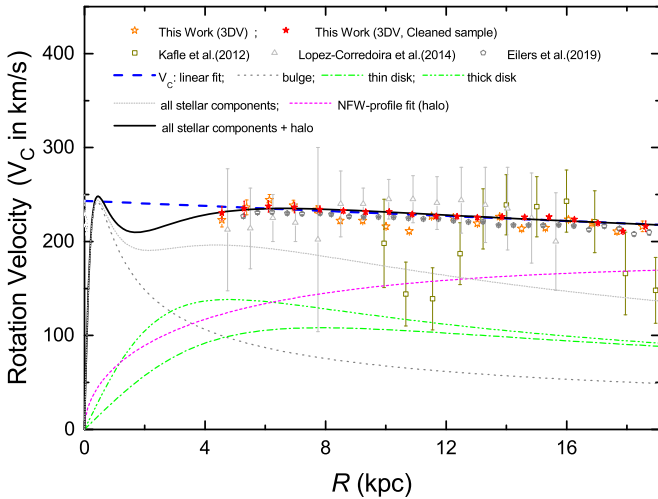

Figure 5. Same as Figure 3, but based on the 3D velocity vector method, and the orange open stars and red filled stars show the results of the all 3D sample and the cleaned sample, respectively.

which is consistent with a similar dip claimed by previous works (Sofue et al. 2009; Kafle et al. 2012; McGauph 2018). However, there is no dip in the results of the cleaned sample with the 3D velocity method (Eilers et al. 2019).

The rotation velocity of the Sun found in the PM method is in good agreement with the results of some previous works (e.g., Bovy et al. 2012; Wegg et al. 2019). The Sun's rotation velocity obtained from the 3D velocity method is, within uncertainties, consistent with the relatively higher values reported by Metezger et al. (1998), Reid et al. (2014), Kawata et al. (2018), and Mróz et al. (2019). The estimated virial masses from the two methods in this work are lower than the values (($\sim$1.0 – $\sim$2.0) $\times$ 10^{12} $M_\odot$) derived by Küpper et al. (2015), Bland-Hawthorn & Gerhard (2016), Watkins et al. (2019), Callingham et al. (2019), and Li et al. (2019). Within

uncertainties, the viral masses in this work are in good agreement with the results of Bovy et al. (2012), Kafle et al. (2012), Eadie et al. (2018), Eadie & Jurić (2019), Eilers et al. (2019), and Cautun et al. (2019). The estimated mass by our 3D velocity method has very good agreement with the mean viral mass (($0.83^{+0.12}_{-0.09}$) $\times$ 10^{12} $M_\odot$) derived by Karukes et al. (2019).

The estimated local dark matter densities from the two methods including the uncertainties are consistent with the values of Weber & de Boer (2010), Sofue (2012), Eilers et al. (2019), and Callingham et al. (2020). However, they are higher than the values ($< \sim$0.2 GeV cm^{-3}) given by Gnaciński (2019), while they are lower than the estimated density ($\sim$0.9 GeV cm^{-3}) by Garbari et al. (2012) and (0.542 $\pm$ 0.042 GeV cm^{-3}) by Bienaymé et al. (2014).

Effect of uncertainties baryonic mass components. The estimation of the dark matter halo profiles relies on observational results of the baryonic mass components. Recently, de Salas et al. (2019) discussed that the dark matter density estimation is more sensitive to the uncertainties of the baryonic components rather than the uncertainties of the rotation velocities. They found a different uncertainty ($\pm$0.149 GeV cm^{-3}) of the dark matter density with the same velocities, and it is about 3 times that of what Eilers et al. (2019) find. They also show that using a different model such as the NFW dark matter profile and Einasto dark matter profile also gives an uncertainty of $\pm$0.036 GeV cm^{-3}. Comparing to the Galactic disk mass in some previous works (e.g., Smith et al. 2007), we took relatively higher masses for the Galactic (thin + thick) disk from Pouliasis et al. (2017). Thus, we may underestimate the halo profiles. We examine it by taking a very simple example, and we run the model by using 5.0 $\times$ 10^{10} $M_\odot$ for the whole disk mass instead of 7.888 $\times$ 10^{10} $M_\odot$ (thin + thick disks) as in this work and from Model I of Pouliasis et al. (2017). We found that the dark matter density goes up to 0.408 GeV cm^{-3} when we reduce the baryonic mass of the Galactic disk in the estimation modeling, and it is 0.078 GeV cm^{-3} higher than the value (0.33 GeV cm^{-3}) derived from Model I of

Pouliasis et al. ([2017](#)). This supports the statement given by de Salas et al. ([2019](#)). Future observational data may provide better constraints on the baryonic components.[5]

Interestingly, the density derived from our 3D velocity method is basically consistent with the estimated dark matter density by de Salas et al. ([2019](#)), which is in a range of (0.3–0.4) GeV cm^{-3}. Our local dark matter density estimated from the 3D velocity method is in very good agreement with the local dark matter density (0.32–0.36 GeV cm^{-3}) inferred from fitting models to the Gaia DR2 Galactic RC and other data (Cautun et al. [2019](#)).

4. Conclusion

We have analyzed 3483 classical Cepheids selected from thousands of classical Cepheids identified by several survey projects (e.g., OGLE, ASAS-SN, Gaia, WISE, and ZTF), and constructed the rotation velocity distribution of the Milky Way between the Galactocentric distances 4 and 19 kpc by using two different methods. The distances of these classical Cepheids have typical uncertainties of <3% (which is crucial in the analysis of the RC), and 3D spatial distributions show a very clear Galactic warp feature claimed by previous works (see the Section [2](#)). By using the PM and 3D velocity methods, 591 and 1078 classical Cepheids have been analyzed, and most of observed uncertainties of PMs and radial velocities are less than 0.2 mas yr^{-1} and 20 km s^{-1}, respectively. This represents the largest classical Cepheid sample analyzed to date. We apply the NFW profile approach to simulate the dark matter content of the Milky Way. Our main findings are:

1. The different methods or/and different sample would give different results to some extent. The uncertainties of baryonic components also have an important role in the estimation of dark matter profiles. The result of the PM method shows that the dark matter halo is the main contributor to the Galactic rotation when the distance $R \gtrsim 14.5$ kpc, while the 3D velocity modeling demonstrates that the Galactic RC is dominated by the dark matter halo at $R \gtrsim 12.5$ kpc. The RCs constructed by both methods are gently declining. The RC from the 3D velocity method is decreasing more gently with a derivative of (-1.33 ± 0.1) km s^{-1} kpc^{-1}. The rotation velocity at the position of the Sun ((233.5 ± 0.83) km s^{-1}) obtained from the 3D velocity method is about 10 km s^{-1} faster than the rotation velocity of the Sun derived from the PM method.

2. The best estimation with the NFW profile based on the RC of the 3D velocity method generates a higher viral mass ($M_{\rm vir} = (0.822 \pm 0.052) \times 10^{12} M_\odot$) with a corresponding radius of $R_{\rm vir} = 191.84 \pm 4.12$ kpc and concentration of $c = 13.04 \pm 0.34$. At the same time, the predicted local dark matter density ($\rho_{\rm DM,\odot} = 0.33 \pm 0.03$ GeV cm^{-3}) is also higher than the estimated value from the PM modeling.

ORCID iDs

Iminhaji Ablimit ● https://orcid.org/0000-0001-7003-4220
Gang Zhao ● https://orcid.org/0000-0002-8980-945X
Chris Flynn ● https://orcid.org/0000-0002-4796-745X

References

Ablimit, I., & Zhao, G. 2017, ApJ, 846, 10
Ablimit, I., & Zhao, G. 2018, ApJ, 855, 126
Bellm, E. C., Kulkarni, S. R., Graham, M. J., et al. 2019, PASP, 131, 018002
Bhattacharjee, P., Chaudhury, S., & Kundu, S. 2014, ApJ, 785, 63
Bienaymé, O., Famaey, B., Siebert, A., et al. 2014, A&A, 571, A92
Binney, J., & Wong, L. K. 2017, MNRAS, 467, 2446
Bland-Hawthorn, J., & Gerhard, O. 2016, ARA&A, 54, 529
Bosma, A., & van der Kruit, P. C. 1979, A&A, 79, 281
Bovy, J. 2015, ApJS, 216, 29
Bovy, J., Allende Prieto, C., Beers, T. C., et al. 2012, ApJ, 759, 131
Bovy, J., & Rix, H.-W. 2013, ApJ, 779, 115
Bowden, A., Belokurov, V., & Evans, N. W. 2015, MNRAS, 449, 1391
Callingham, T. M., Cautun, M., Deason, A. J., et al. 2019, MNRAS, 484, 5453
Callingham, T. M., Cautun, M., Deason, A. J., et al. 2020, arXiv:2001.07742
Cautun, M., Benitez-Llambay, A., Deason, A. J., et al. 2019, arXiv:1911.04557
Chen, X. D., Wang, S., Deng, L. C., et al. 2020, ApJS, submitted
Chen, X. D., Wang, S., Deng, L. C., et al. 2019, NatAs, 3, 320
de Salas, P. F., Malhan, K., Freese, K., Hattori, K., & Valluri, M. 2019, JCAP, 2019, 037
Deason, A. J., Belokurov, V., & Sanders, J. L. 2019, arXiv:1912.02599v2
Dubinski, J. 1994, ApJ, 431, 617
Eadie, G., & Jurić, M. 2019, ApJ, 875, 159
Eadie, G. M., Keller, B., & Harris, W. E. 2018, ApJ, 865, 72
Eilers, A.-C., Hogg, D. W., Rix, H.-W., & Ness, M. 2019, ApJ, 871, 120
Flynn, C., Holmberg, J., Portinari, L., et al. 2006, MNRAS, 372, 1149
Freeman, K. C. 1970, ApJ, 160, 811
Frink, S., Fuchs, B., & Wielen, R. 1995, AGAb, 11, 196
Gaia Collaboration, Aburter, R., Amorim, A., et al. 2018, A&A, 615, L15
Gaia Collaboration, Prusti, T., de Bruijne, J. H. J., et al. 2016, A&A, 595, A1
Garbari, S., Liu, C., Read, J. I., & Lake, G. 2012, MNRAS, 425, 1445
Gnaciński, P. 2019, AN, 340, 787
Grand, R. J. J., Kawata, D., & Cropper, M. 2014, MNRAS, 439, 623
Gravity Collaboration, Aburter, R., Amorim, A, et al. 2018, A&A, 615, L15
Gunn, J. E., Knapp, G. R., & Tremaine, S. D. 1979, AJ, 84, 1181

---

[5] Note that previous works made important progress in modeling the baryon budget of the Galactic disk and its uncertainties (e.g., Flynn et al. [2006](#); Bovy & Rix [2013](#)).

Honma, M., Bushimat, T., Choi, Y. K., et al. 2007, PASJ, 59, 889
Ibata, R., Lewis, G. F., Irwin, M., Totten, E., & Quinn, T. 2001, ApJ, 551, 294
Jayasinghe, T., Stanek, K. Z., Kochanek, C. S., et al. 2018, arXiv:1809.07329
Kafle, P. R., Sharma, S., Lewis, G. F., & Bland-Hawthorn, J. 2012, ApJ, 761, 98
Kafle, P. R., Sharma, S., Lewis, G. F., & Bland-Hawthorn, J. 2014, ApJ, 794, 59
Karukes, E. V., Benito, M., Iocco, F., et al. 2019, arXiv:1912.04296v1
Katz, D., Antoja, T., et al. 2018, A&A, 616, A11
Kawata, D., Bovy, J., Matsunaga, N., & Baba, J. 2018, MNRAS, 482, 40
Küpper, A. H. W., Balbinot, E., Bonaca, A., et al. 2015, ApJ, 803, 80
Lake, G. 1989, AJ, 98, 1554
Levine, E. S., Heiles, C., & Blitz, L. 2008, ApJ, 679, 1288
Li, Z. Z., Qian, Y. Z., Han, J., et al. 2019, arXiv:1912.02086v1
López-Corredoira, M., Abedi, H., Garzón, F., & Figueras, F. 2014, A&A, 572, A101
Lux, H., Read, J. I., Lake, G., & Johnston, K. V. 2012, MNRAS, 424, L16
Martinez-Medina, L., Pichardo, B., Peimbert, A., & Valenzuela, O. 2019, MNRAS, 485, L105
McGaugh, S. S. 2018, RNAAS, 2, 156
Medina, G. E., Munoz, R. R., Vivas, A. K., et al. 2018, ApJ, 855, 43
Mel'nik, A. M., Rautiainen, P., Berdnikov, L. N., Dambis, A. K., & Rastorguev, A. S. 2015, AN, 336, 70
Metezger, M. R., Caldwell, J. A. R., & Schechter, P. L. 1998, ApJ, 115, 635
Miyamoto, M., & Nagai, R. 1975, PASJ, 27, 533
Monari, G., Famaey, B., Carrillo, I., et al. 2018, A&A, 616, L9
Mróz, P., Udalski, A., Skowron, D. M., et al. 2019, ApJL, 870, L10
Navarro, J. F., Frenk, C. S., & White, S. D. M. 1996, ApJ, 462, 563
Navarro, J. F., Frenk, C. S., & White, S. D. M. 1997, ApJ, 490, 493
Nesti, F., & Salucci, P. 2013, JCAP, 07, 016
Pato, M., & Iocco, F. 2017, SoftX, 6, 54
Plummer, H. C. 1911, MNRAS, 71, 460

Pont, F., Queloz, D., Bratschi, P., & Mayor, M. 1997, A&A, 318, 416
Pouliasis, E., Di Matteo, P., & Haywood, M. 2017, A&A, 598, 66
Read, J. I., Lake, G., Agertz, O., & Debattista, V. P. 2008, MNRAS, 389, 1041
Reid, M. J., Menten, K. M., Brunthaler, A., et al. 2014, ApJ, 783, 130
Reid, M. J., Menten, K. M., Zheng, X. W., et al. 2009, ApJ, 700, 137
Ripepi, V., Molinaro, R., Musella, I., et al. 2019, A&A, 625A, 14R
Russeil, D., Zavagno, A., Mege, P., et al. 2017, A&A, 601, L5
Schönrich, R., Binney, J., & Dehnen, W. 2010, MNRAS, 403, 1829
Shappee, B. J., Prieto, J. L., Grupe, D., et al. 2014, ApJ, 788, 48
Skowron, D. M., Skowron, J., Mroz, P., et al. 2019a, Sci, 365, 478
Skowron, D. M., Skowron, J., Mroz, P., et al. 2019b, AcA, 69, 305
Smith, M. C., Ruchti, G. R., Helmi, A., et al. 2007, MNRAS, 379, 755
Sofue, Y. 2012, PASJ, 64, 75
Sofue, Y., Honma, M., & Omodaka, T. 2009, PASJ, 61, 227
Sohn, S. T., Watkins, L. L., Fardal, M. A., et al. 2018, ApJ, 862, 52
Stibbs, D. W. N. 1955, MNRAS, 115, 363
Udalski, A., Soszyński, I., Pietrukowicz, P., et al. 2018, AcA, 68, 315
Udalski, A., Szymański, M. K., & Szymański, G. 2015, AcA, 65, 1
Utkin, N. D., Dambis, A. K., Rastorguev, A. S., et al. 2018, AstL, 44, 688
van Albada, T. S., Bahcall, J. N., Begeman, K., & Sancisi, R. 1985, ApJ, 295, 305
Volders, L. M. J. S. 1959, BAN, 14, 323
Wang, W. T., Han, J. X., Cole, S., et al. 2018, MNRAS, 476, 5669
Watkins, L. L., van der Marel, R. P., Sohn, S. T., & Evans, N. W. 2019, ApJ, 873, 118
Weber, M., & de Boer, W. 2010, A&A, 509, A25
Wegg, C., Gerhard, O., & Bieth, M. 2019, MNRAS, 485, 3296
Wilkinson, M. I., & Evans, N. W. 1999, MNRAS, 310, 645
Wright, E. L., Eisenhardt, P. R. M., Mainzer, A. K., et al. 2010, AJ, 140, 1868
Zhao, G., Chen, Y.-Q., Shi, J.-R., et al. 2006, ChJAA, 6, 265
Zhao, G., Zhao, Y. H., Chu, Y. Q., et al. 2012, RAA, 12, 723